**Supplementary Information for**

# Modulation of the Photo-response of $SrTiO_3$: Insights of Surface Defect on Solid Oxide Photoelectrochemical Cell

*Luyao Wang,[a] Jifang Zhang,[a] Xinyu Zhang,[a] Guijun Ma*[a] and Nan Yang*[a]*

[a] School of physical science and technology, ShanghaiTech University, Shanghai 201210, P.R. China

*** Corresponding Author**

E-mail:

magj@shanghaitech.edu.cn

nan.yang2018@gmail.com

## Experimental section

### Design of the device models

$La_{0.9}Sr_{0.1}Ga_{0.95}Mg_{0.05}O_{3-\delta}$ (LSGM) thin films were deposited by PLD on double side polished (100)-oriented $SrTiO_3$ (STO) single crystal substrates (substrate size is 10*10*0.1 $mm^2$). Targets were prepared from commercial LSGM powders (Praxair), by uniaxially pressing at 10 MPa and sintering at 1200 °C for 10 h. The KrF excimer pulsed laser source ($\lambda$ = 248 nm) was operated at 10 Hz, with an energy density of 150 $mW \cdot cm^{-2}$. The substrate temperature was set as 750 °C and $O_2$ pressure was set as 10 mtorr. The distance between target and substrate was 60 mm [1]. The Pt thin films were prepared by magnetron sputtering under 20 mtorr Ar gas at room temperature on the LSGM as the anode and on the STO as the current collector. The power was 100 W.

### X-ray photoelectron spectroscopy (XPS)

X-ray photoemission spectroscopy measurements were performed on a Thermo Scientific K-Alpha+ equipped with a Mono Al Kα source. The X-ray source energy was 1486.6 eV that corresponds to an electron inelastic mean free path for samples of about 2.4 nm.

### Atomic force microscopy (AFM)

The surface morphology of the thin films was examined using atomic force microscopy (AFM). Topographic images were acquired under dry conditions in tapping mode with silicon cantilevers at approximately 300 kHz, using a Dimension Icon AFM equipped with a Nanoscope V controller (Digital Instruments, Goleta, CA, USA).

### Measurement set-up for the fuel cell test

A specifically designed reactor was applied for the solid oxide photoelectrochemical cell (SOPECs) measurements. The reactor is separated into an upper and a lower chamber by a middle sample loading plate. There is a circular transparent window on the top of the upper chamber, and the window is equipped with quartz glass to allow UV light to pass through. The reactor is equipped with a heating system and a gas flow

system to ensure a safe operation within a temperature range of 500-1000 °C in different gas environments.

**S1: Morphological information of LSGM thin films deposited on STO substrates.**

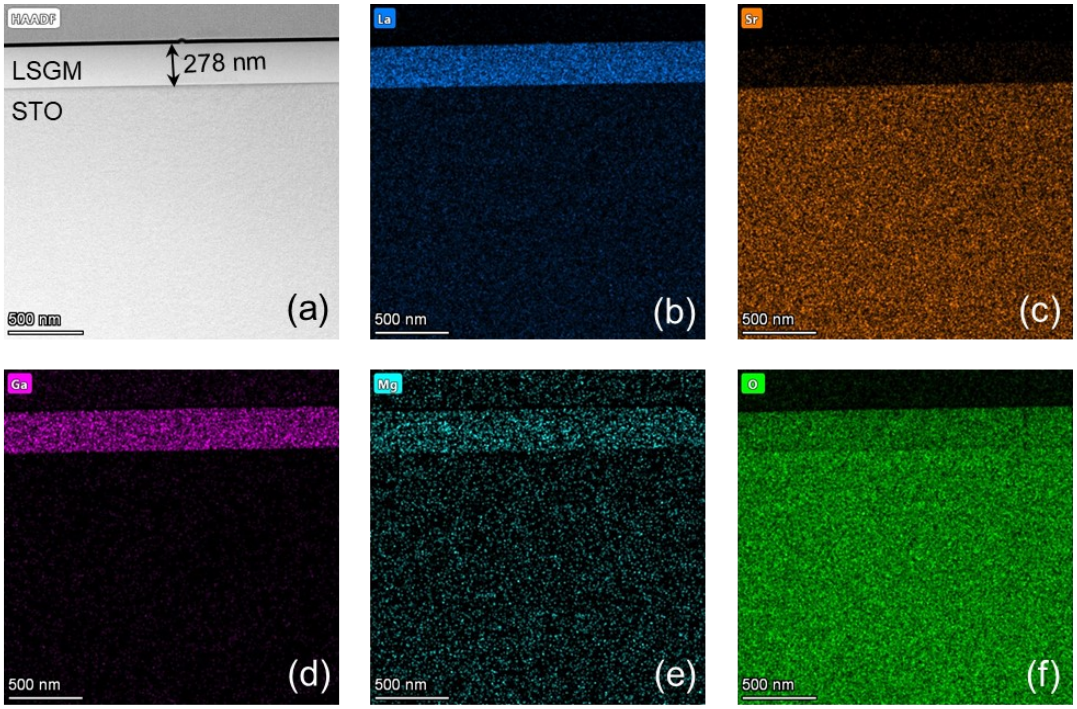


**Figure S1.** (a) High-angle annular dark-field (HAADF) images of the cross-section view of LSGM thin films deposited on STO substrates and EDS mappings of (b) La, (c) Sr, (d) Ga, (e) Mg and (f) O elements.

**S2: X-ray photoelectron spectroscopy (XPS).**

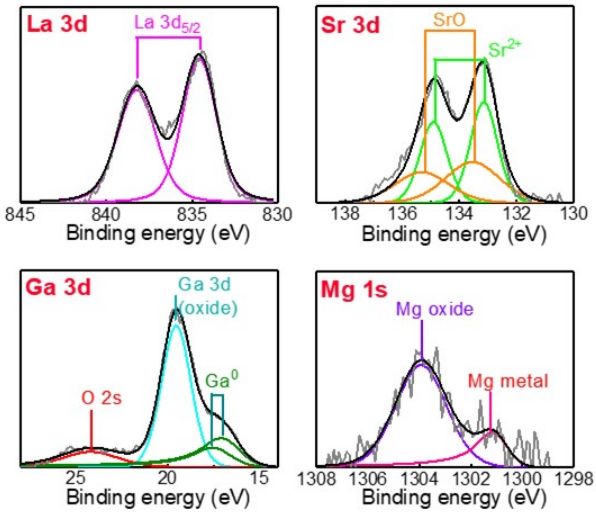


**Figure S2.** La 3d, Sr 3d Ga 3d and Mg 1s spectra of the LSGM thin films. The XPS measurements were performed on a Thermo Fisher ESCALAB 250XI equipped with an Al Kα source. The x-ray source energy was 1486.74 eV that corresponds to an electron inelastic mean free path for samples of about 2.4 nm.

**S3: Fuel cell test of Pt-STO||LSGM||Pt single cell at various temperatures.**

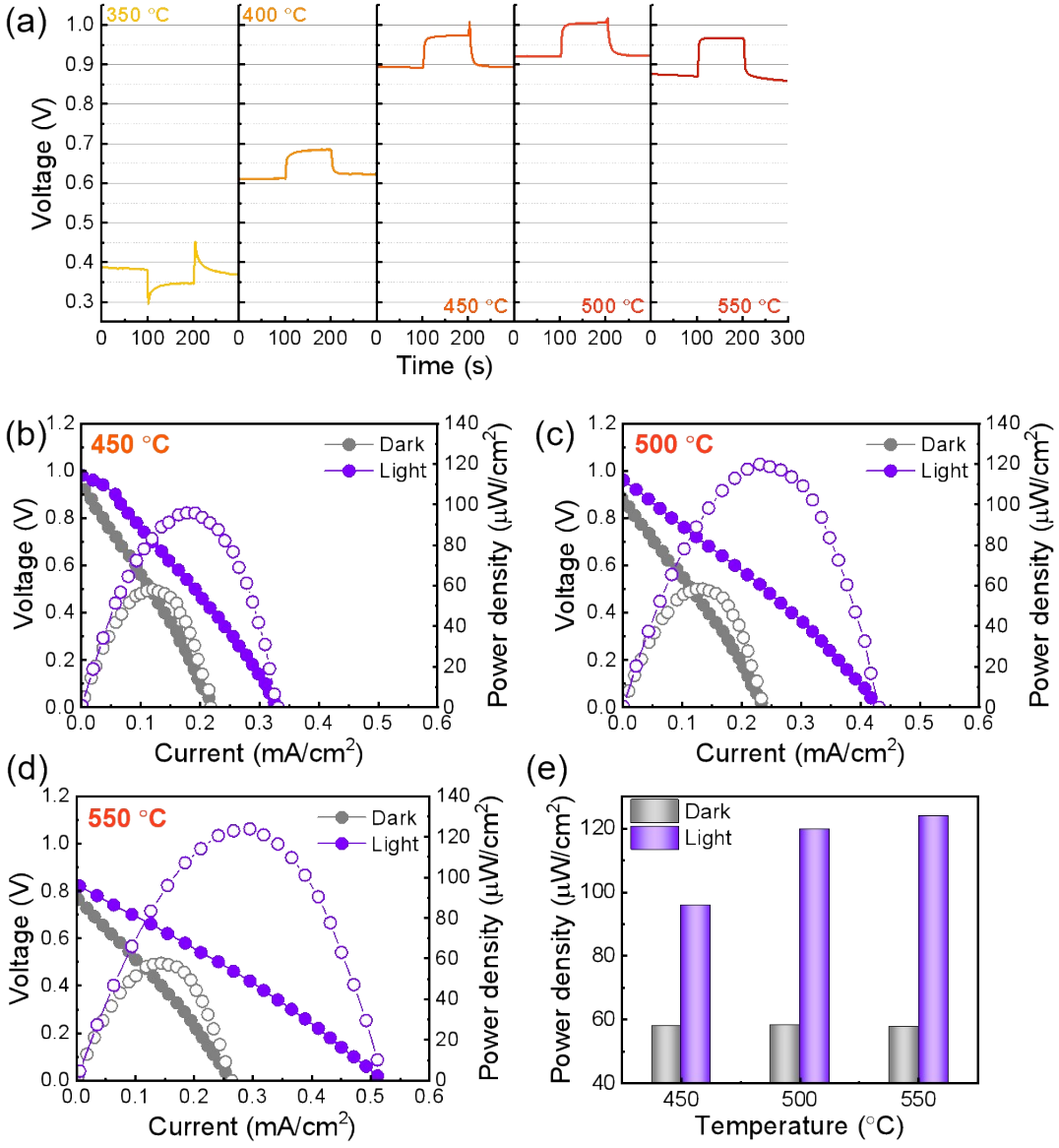


**Fig. S3** (a) The OCV plots. The UV light was turned on at 100 s and turned off at 200 s. The U-I polarization curves collected at (b) 450, (c) 500 and (d) 550 °C. (e) Comparison of the peak power density of the SOPEC under fuel cell operation mode at different temperatures.

Fuel cell tests were performed on the Pt-STO||LSGM||Pt configuration at various temperatures. The OCV curves were collected across a temperature range of 350-550 °C, as shown in Fig. S3a. At 350 and 400 °C, the development of the Nernst voltage is extremely slow due to

substantial activation overpotential and diffusion limitations. Reliable OCV values are first observed at 450 °C, peaking at 500 °C, and followed by a slight decline at 550 °C. Interestingly, the photovoltages remain relatively stable across the 450, 500 and 550 °C.

Additionally, polarization curves were measured at different temperatures to further assess SOPEC performance. Higher temperatures significantly enhance the ionic conductivity of SOPECs, leading to a considerable increase in peak power density under UV illumination at 500 °C compared to 400 °C. However, as the temperature rises to 550 °C, no further substantial improvement in peak power density is observed. Based on these results, 500 °C was selected as the optimal test temperature for subsequent experiments.

**S4: Distribution of Relaxation Times (DRT) analysis.**

Relaxation time distribution is an Electrochemical Impedance Spectroscopy (EIS) analysis technique that does not rely on prior knowledge of the studied object[2]. It can separate and analyze highly overlapped physical and chemical processes in EIS. This technique has been widely used in the field of electrochemical energy, particularly for the diagnosis and optimization of fuel cell device performance[3–5]. The main objective of the DRT is to determine the characteristic distribution of time scales for typical EIS. In order to achieve this, the experimental data $Z_{exp}$ measured at a given frequency were "fitted" to the model $Z_{DRT}$, which is obtained from the following expression[6]:

$$Z_{DRT}(f) = R_{\infty} + \int_{0}^{\infty} \frac{g(\tau)}{1 + i2\pi f\tau} d\tau$$

Where $R_{\infty}$ is the ohmic resistance, $f$ is the frequency, $\tau$ is the relaxation time, and $g(\tau)$ is an appropriate function describing the time relaxation characteristics of the electrochemical system. The impedance of the DRT model is composed of the sum of an ohmic resistance and an infinite series of parallel resistors and capacitors, which can be understood as an equivalent Voigt circuit. In this work, DRT was performed with DRT tools [6]. The regularization parameter was set as 5 $x10^{-3}$ and the full width at half maximum (FWHM) of the radial basis functions (RBFs) used for discretization was 0.2.

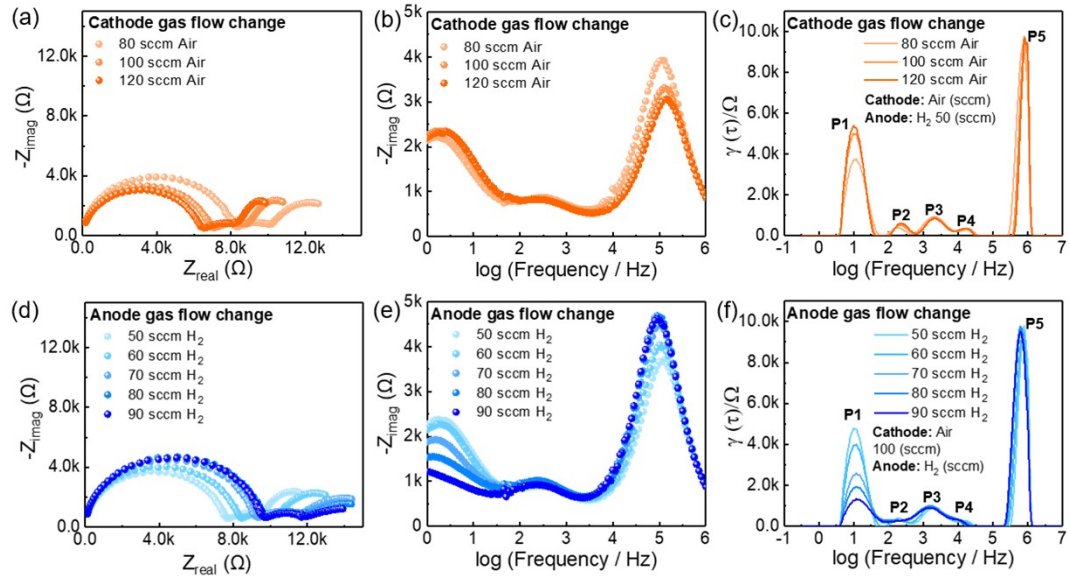


**Figure S4.** (a), (d) Nyquist plots, (b), (e) Bode plots of EIS spectra, and (c), (f) DRT results as functions of the Air flow at the cathode and the $H_2$ flow at the anode at 510 °C based on the Pt-STO||LSGM||Pt cell (The thickness of the STO substrate was 0.2 mm). (a), (b) and (c) were correspond to the variation in the Air flow at the cathode. (d), (e) and (f) were correspond to the variation in $H_2$ flow at the anode.

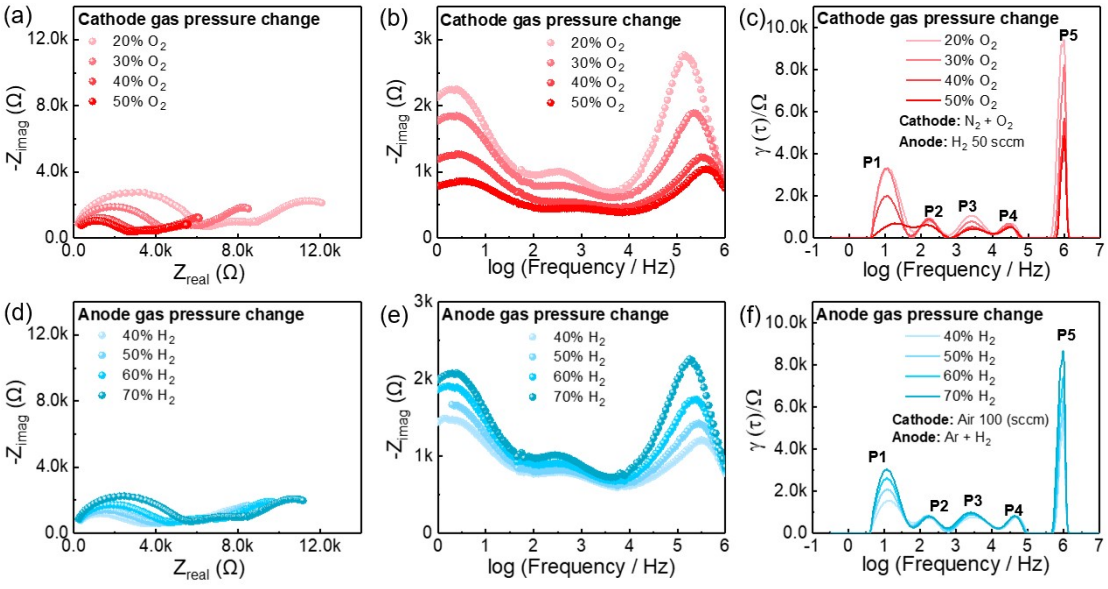


**Figure S5.** (a), (d) Nyquist plots, (b), (e) Bode plots of EIS spectra, and (c), (f) DRT results as functions of the $O_2$ partial pressure at the cathode and the $H_2$ partial pressure at the anode at 510 °C based on the Pt-STO||LSGM||Pt cell (The thickness of the STO

substrate was 0.2 mm). (a), (b) and (c) were correspond to the variation in the $O_2$ partial pressure at the cathode. (d), (e) and (f) were correspond to the variation in $H_2$ partial pressure flow at the anode.

**S5: The bulk conductivity facilitated by UV illumination.**

The photoelectrochemical impedance spectroscopy (PEIS) characterization was carried out for the Pt-STO||Pt reference sample and Pt-STO||LSGM||Pt SOPEC device under fuel cell operation. The conductivity changing with the temperature range from 400 to 500 °C was plotted in Fig. S6a-b, and the activation energy ($E_a$) was also analyzed from the Arrhenius plots. The conductivity was calculated by fitting the first semicircle in the Nyquist plot (the red portion). There were four phenomena that deserve special attention: (i) At 500 °C, in the dark state, compared with the Pt-STO||Pt, the conductivity of Pt-STO||LSGM||Pt dropped sharply from $1.7 \times 10^{-5}$ to $9.7 \times 10^{-6}$ S · cm$^{-1}$. (ii) The $E_a$ of the Pt-STO||Pt reference sample in the dark state is 0.68 eV. After the introduction of the LSGM layer, the $E_a$ of the Pt-STO||LSGM||Pt were 0.83 eV, showing a significant increase compared to the reference sample. Since the $E_a$ of LSGM thin films was generally between 0.65 and 0.75 eV[7], which was also much lower than the $E_a$ of the model devices. It can be inferred that the increase in the $E_a$ of the model devices is independent of the ionic conduction within the bulk of LSGM layer. (iii) Under UV illumination, the conductivity of both two samples increased, especially for the Pt-STO||LSGM||Pt with LSGM electrolyte layers. At 500 °C, the conductivity of Pt-STO||LSGM||Pt increased from $9.7 \times 10^{-6}$ to $2.8 \times 10^{-5}$ S · cm$^{-1}$ after the UV light was turned on. This result was consistent with the flattened slope of the I-V curve with UV illumination in Fig. 1e. (iv) Finally, the $E_a$ of the Pt-STO||Pt reference sample slightly decreased from 0.68 to 0.58 eV after UV light was turned on. The decrease in the $E_a$ of STO single crystals was attributed to the UV light-driven oxygen incorporation reaction that reduces the concentration of oxygen vacancy defects in STO, making electronic conduction more favorable [8]. However, the $E_a$ of the SOPEC device under UV light were 0.52 eV, which was a significant decrease and was very close to the $E_a$ of the reference sample. This cannot be simply explained by the changes in the amount of the photo-excited electrons in STO. Based on the above experimental phenomena, it can be concluded that after the introduction of the LSGM layer, the rate-determining step of the ionic and electronic conduction has changed, resulting in a decrease in the

conductivity and a significant increase in the $E_a$ in the dark state. We believed that the interface between the STO photoelectrode and the LSGM electrolyte, and its induced polarization resistance, were the main reasons for the increased $E_a$ of the model device. UV irradiation seemed to be able to eliminate the effect of polarization resistance brought by the photoelectrode/electrolyte interface, making the conductivity and $E_a$ of the Pt-STO||LSGM||Pt model devices very close to that of the STO bulk (Fig. S6e).

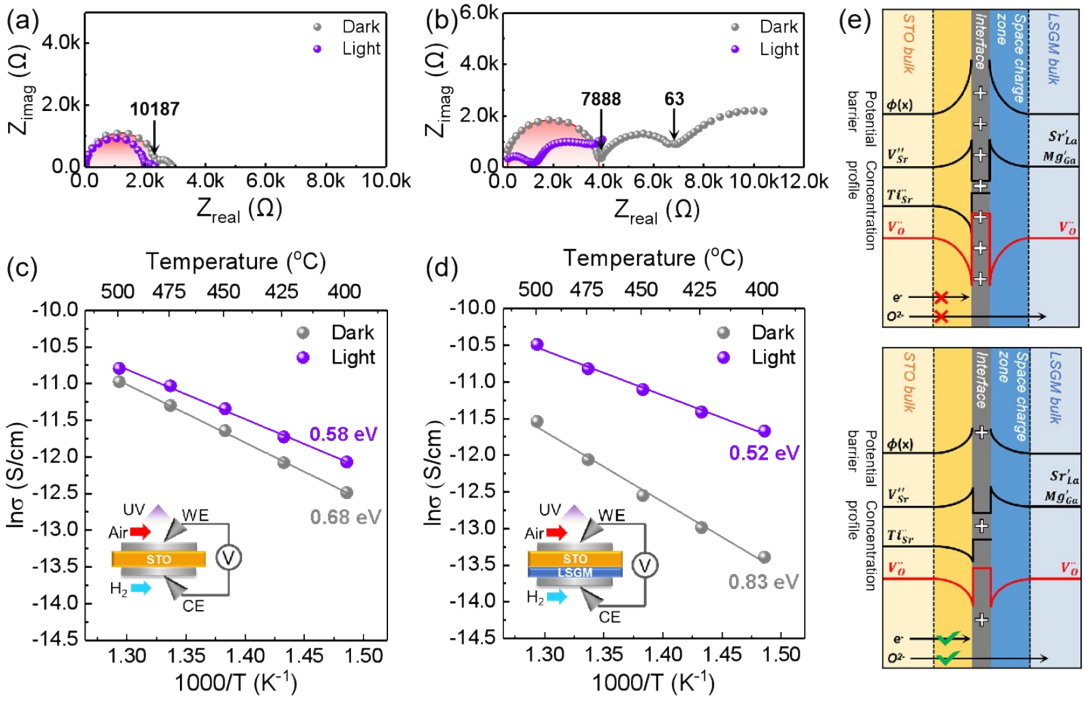


**Fig. S6** PEIS results for Pt-STO||Pt reference sample (a, c), Pt-STO||LSGM||Pt (b, d) at 500 ˚C with hydrogen as fuel and air as oxidant. (a, b) the Nyquist plots. (c, d) Arrhenius plots. The conductivity was obtained by fitting the first semicircle (the red portion) in the Nyquist plots. (e) The schematics of the conductivity enhancement of Pt-STO||LSGM||Pt under UV light. The top portion is the STO||LSGM interface in the dark state and the bottom portion is the STO||LSGM interface under UV illumination.

**S6: The polarization process of the Pt-STO||LSGM||Pt devices models.**

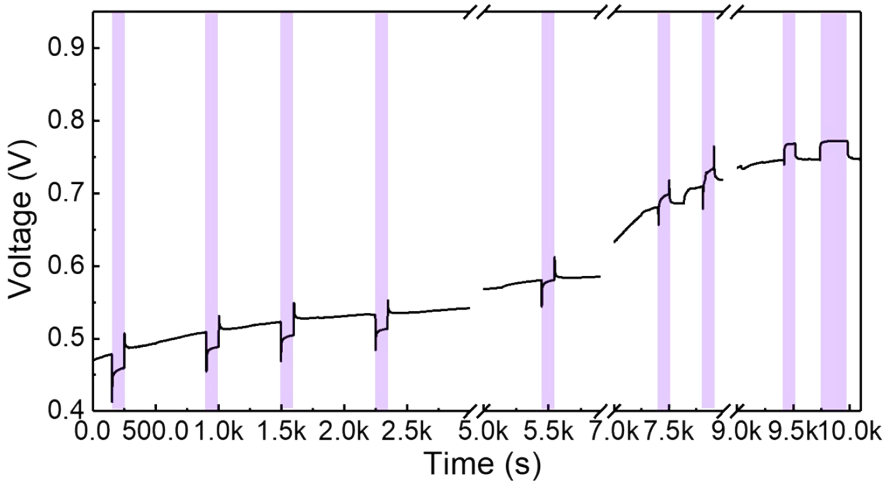


**Figure S7.** OCV test results of the Pt-STO||LSGM||Pt cell (The thickness of the STO substrate was 0.2 mm) at 500 °C in an asymmetric atmosphere of Air||$H_2$ on a long-time scale.

**S7: Pt-STO||Pt solid oxide solar cell.**

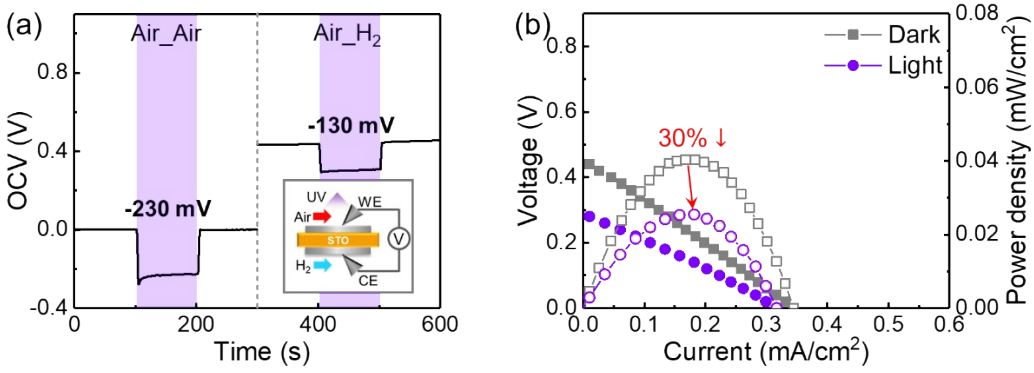


**Figure S8.** (a) The OCV plots. The purple aregion indicated that the UV light was turned on. The inserted picture showed the sample structure and the measurement set-up. (b) The U-I polarization curves. The testing temperature was 500 °C. The air flow on the STO side was 100 sccm, and the $H_2$ flow on the LSGM side was 50 sccm.

**S8: Surface modification with the protective layer.**

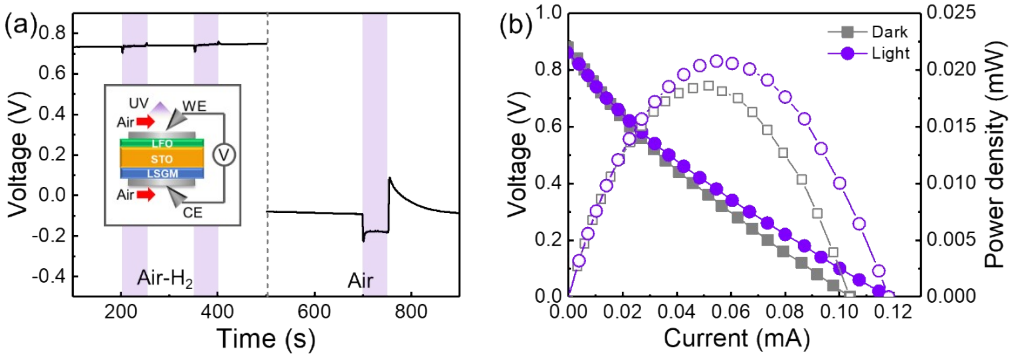


**Fig. S9** (a) OCV curve of Pt-LFO-STO||LSGM||Pt samples at 500 °C under both the fuel cell operation and the atmospheric. (b) The U-I curve under the Air_$H_2$ asymmetric atmosphere.

**S9: The atomic ratio calculation of Sr/Ti through fitting of XPS spectrum.**

The atomic ratios of Sr and Ti in the STO lattice can be calculated using the following equation:

$$Sr/Ti = Area\ of\left[\frac{Sr\ 3d_{5/2}/2.99 + Sr\ 3d_{3/2}/2.06}{Ti\ 2p_{3/2}/5.22 + Ti\ 2p_{1/2}/2.69}\right]$$

where 2.99 and 2.06 are the relative sensitivity factors (RSFs) for Sr 3*d* core level, while 5.22 and 2.69 are the RSFs for Ti 2*p* core level. The fitting results and the calculated atomic ratio are listed in Table S1. It is evident that the Sr/Ti ratio of Pt-STO(HV)||LSGM||Pt is close to 1, indicating a low concentration of Sr vacancies. And after the fuel cell test, its Sr/Ti ratio decreased slightly to 0.81, consistent with the observation that the $SrO_{1+x}$% on the surface of the Pt-STO(HV)||LSGM||Pt did not significantly increase. In contrast, the Sr/Ti ratio of Pt-STO||LSGM||Pt dropped sharply to 0.46 after the fuel cell test, the generation of a substantial number of Sr vacancies on the surface.

Table S1. Sr/Ti atomic ratio obtained by fitting Sr 3*d* and Ti 2*p* core level spectra.

| | | Area | | | | atomic ratio of Sr/Ti |
|---|---|---|---|---|---|---|
| | | Sr $3d_{5/2}$ | Sr $3d_{3/2}$ | Ti $2p_{3/2}$ | Ti $2p_{1/2}$ | |
| Pt-STO\|\|LSGM\|\|Pt | Before test | 60578 | 40930.5 | 63758.4 | 51910.5 | 1.27 |
| | After test | 3877.1 | 2600 | 12298 | 8700.3 | 0.46 |
| Pt-STO(HV)\|\|LSGM\|\|Pt | Before test | 40224 | 26817 | 54399 | 41796 | 1.02 |
| | After test | 34966.5 | 24342.3 | 66842 | 43302 | 0.81 |

**Reference:**


1 N. Yang, A. D'Epifanio, E. Di Bartolomeo, C. Pugnalini, A. Tebano, G. Balestrino and S. Licoccia, *J. Power Sources*, 2013, **222**, 10–14.

2 M. A. Danzer, *Batteries*, 2019, 5.

3 C. Endler, A. Leonide, A. Weber, F. Tietz and E. Ivers-Tiffée, *J. Electrochem. Soc.*, 2010, **157**, B292.

4 Y. Wang, N. Xu, E. Dogdibegovic, T. Su, A. D. Brocato and X.-D. Zhou, *Int. J. Hydrogen Energy*, 2022, **47**, 1917–1924.

5 Z. Zheng, J. Jing, Z. Lei, Z. Wang, Z. Yang, C. Jin and S. Peng, *Int. J. Hydrogen Energy*, 2022, **47**, 18139–18147.

6 T. H. Wan, M. Saccoccio, C. Chen and F. Ciucci, *Electrochim. Acta*, 2015, **184**, 483–499.

7 R. Gao, A. C. P. Jain, S. Pandya, Y. Dong, Y. Yuan, H. Zhou, L. R. Dedon, V. Thoréton, S. Saremi, R. Xu, A. Luo, T. Chen, V. Gopalan, E. Ertekin, J. Kilner, T. Ishihara, N. H. Perry, D. R. Trinkle and L. W. Martin, *Adv. Mater.*, 2020, **32**, 1905178.

8 A. Viernstein, M. Kubicek, M. Morgenbesser, T. M. Huber, E. Ellmeyer, M. Siebenhofer, C. A. F. Vaz and J. Fleig, *Solid State Ionics*, 2022, **383**, 115992.